Computational Studies of Amoeboid Cell Motility in Three-dimensional Matrices

Y. Sakamoto[a], S. Prudhomme[a], and M.H. Zaman[b]

[a] *Institute for Computational Engineering and Sciences, The University of Texas at Austin*
1 University Station, Austin, TX 78712, USA

[b] *Department of Biomedical Engineering, Boston University*
44 Cummington Street, Boston, MA 02215, USA

September 28, 2009

Abstract

Tumor cells, upon loss of integrins or proteolytic machinery, are able to navigate through complex matrices through adhesion-independent or amoeboid mechanism. While adhesion dependent migration has been studied in both 2D and 3D environments, quantitative models of amoeboid motion in native environments are lacking. We have developed two- and three-dimensional models of an amoeboid cell crawling through extracellular matrix (ECM) gaps using the finite element method. The model provides a powerful tool for the analysis of interactions between a cell and extracellular matrix and fluids in vitro and in vivo. The cell is modeled as an incompressible Newtonian fluid with surface tension on its boundary, where the chemotactic gradient induces the cell migration through a micro-channel. The relationships among the speed of the cell, diameter of a hole with respect to a size of the cell, the strength of the gradient, surface tension, and viscosity of the fluid inside/outside of the cell are calculated. Our results highlight the dependence of overall speed on both internal and external mechano-chemical gradients, predict the centroid speed in 3D micro-channels and provide a quantitative framework to develop a fundamental understanding of complex cell motion in 3D environments.

1 Introduction

1.1 Significance and Motivation

Tumor metastasis is the process by which cancer spreads from one part of the body to another. The invasion of the tumor cells involve with the coordinated adhesion, proteolytic interaction with the extracelullar matrix (ECM), which degrades and remodels the tissue barriers, and migration through dense environments [10]. Recent studies suggest that inhibition of the ECM-degrading enzymes results in a flexible amoeba-like morphology in a variety of the tumor cells, which is characterized by the protrusion into preexisting matrix gaps and formation of constriction rings [25]. Therefore, identification of crucial factors regulating tumor cell motility in the absence of MMP activity or reduced integrin expression has profound implications for curing cancer and controlling cancer progression and dissemination [6, 8, 7, 26, 27].

Research performed over the last two decades depict a number of mechanisms responsible for migration of the cells exhibiting amoeba-like behavior, which includes not only tumor cells, but also

fibroblasts, macrophages, and leukocytes [14, 21, 22, 23, 28]. However, two fundamental problems characterize these studies and critically hamper our understanding of cell migration. First, almost all of these experiments and simulations were carried out on artificial two-dimensional substrates, which are significantly different from the environment that characterizes the in vivo state. In 2D, cells exhibit flattened morphology migrating slowly on substrates without any matrix resistance or complex proteolytic interactions. On the other hand, in a 3D environment, cells exhibit dynamic changes in its morphology in order to crawl through matrix gaps [26]. Second, while we know how individual factors such as integrins, matrix structure, ECM-degrading enzymes, and spindle fibers contribute individually to the cell motility, we lack the understandings of how these factors jointly regulate the motility.

1.2 Mathematical Models

In recent years, numerous mathematical and computational models have been developed to improve our understanding of the various aspects of cell motility. These models include reaction-diffusion type models to describe kinetics and reactions, ordinary differential equation models for various signaling pathways [20], molecular dynamics models to account for the molecular motors and molecules at the cell-matrix interface [16, 24], continuum mechanics models to describe the force generation and dissipation in various positions in migrating cells [15, 19, 1], or Monte Carlo and other probabilistic models for cell-cell and cell-matrix interactions [30, 29, 31]. These approaches have been extremely useful in providing quantitative frameworks for existing experimental data, for resolving contradictions in experimental literature, for making a priori predictions, and for suggesting a series of new experiments to develop a richer understanding of processes underlying cell migration at various length and time scales.

However, models describing migration of a whole cell in a three-dimensional matrix are lacking [17]. One reason for this lack of three-dimensional models is due to inadequate experimental data to support or validate the 3D modeling results. A new generation of detailed 3D migration models would give us nevertheless a better understanding of cell migration in native-like environments. Therefore, three-dimensional axisymmetric models of an amoeboid cell crawling through ECM gaps are developed and discretized using the finite element method. The models provide very promising tools for analysis of the interaction between a cell and extracellular matrix and fluids in vitro and in vivo.

2 Modeling of Cell Migration

The objective of this work is to provide a quantitative framework to model the migration of an amoeboid cell through a micro-channel induced by a chemotactic gradient, as described in Fig. 1. These scenarios are often encountered by cells migrating without anchorage or proteolytic machinery in complex 3D environments. For the purposes of our simulation, the cell is composed of the nucleus and cytosol and is immersed in a given extracellular fluid. The flow in the cytosol and in the extracellular fluid is assumed to be incompressible because of the aqueous nature of the fluid and the very slow motion. The nucleus is considered as non-deformable body, as seen in recent studies performed using force probes. For the sake of simplicity, we will model it as a fluid with a very large viscosity. Assuming that the cell and extracellular fluid occupy the domain $D \subset \mathbb{R}^3$ and that the motion is evaluated in the time interval $[0, T]$. Migration of the cell within the fluid is governed

by the incompressible Navier-Stokes equations:

$$\rho\frac{\partial \mathbf{u}}{\partial t} + \rho\mathbf{u}\cdot\nabla\mathbf{u} + \nabla p - \nabla\cdot 2\mu\,\mathbb{E}(\mathbf{u}) = \mathbf{f} \qquad \text{in } D\times(0,T) \tag{1}$$

$$\nabla\cdot\mathbf{u} = 0 \qquad \text{in } D\times(0,T) \tag{2}$$

where $\mathbf{u}$ is the velocity field, p is the pressure, $\mathbf{f}$ represents body forces, ρ is the fluid density, μ is the dynamic viscosity, and $\mathbb{E}(\mathbf{u})$ is the rate-of-strain tensor defined as:

$$\mathbb{E}(\mathbf{u}) = \frac{1}{2}\big(\nabla\mathbf{u} + (\nabla\mathbf{u})^T\big) \tag{3}$$

The governing equations will be supplemented below by adequate initial and boundary conditions.

We furthermore make the folllowing assumptions: 1) the fluid follows a Newtonian constitutive relationship; 2) the Reynolds number is sufficiently small so that the advective term, $\rho\mathbf{u}\cdot\nabla\mathbf{u}$ is negligible; 3) the body forces are identically zero, i.e. $\mathbf{f} = \mathbf{0}$; 4) the inertial forces, $\rho\,\partial_t\mathbf{u}$ are also considered negligible with respect to the pressure and viscous contributions. The last assumption suggests to integrate in time the system of equations as a quasi static process, that is, that the system goes through a sequence of states that are infinitesimally close to equilibrium. We note however that the configuration of the domain shall change at each instant of time $t\in[0,T]$, i.e. $D = D(t)$, since the cell will move within the extracellular fluid. Based on all these assumptions, the Navier-Stokes equations (1)–(2) can be reduced to the time-independent Stokes equations to be solved at each time $t\in(0,T]$:

$$-\mu\Delta\mathbf{u} + \nabla p = \mathbf{0} \qquad \text{in } D(t) \tag{4}$$

$$\nabla\cdot\mathbf{u} = 0 \qquad \text{in } D(t) \tag{5}$$

where Δ is the Laplacian operator defined as $\Delta(\cdot) = \nabla\cdot\nabla(\cdot)$. The flows in the cell and extracellular fluid are governed by these equations; however, because the cell migrates in the fluid, the geometries of the cell and nucleus need to be updated at each time. We will employ an Arbitrary Lagrangian-Eulerian approach (ALE) to predict the evolution of the cell position.

We will also assume that the initial state of the cell (nucleus and cytosol) and external geometry, as well as the loadings and boundary conditions are axisymmetric; the three-dimensional problem of interest can then be reduced to a two-dimensional problem as shown below.

2.1 Governing Equations

Let $\Omega\in\mathbb{R}^2$ be the open bounded domain shown in Fig. 2 with boundary $\partial\Omega$. At a given time $t\in[0,T]$, the domain Ω can be decomposed into three open subdomains Ω_i, $i = 1,2,3$ such that subdomain $\Omega_1(t)$ is occupied by the cell nucleus, $\Omega_2(t)$ by the cytosol, and $\Omega_3(t)$ by the extracellular fluid. We thus have

$$\overline{\Omega(t)} = \overline{\Omega_1(t)\cup\Omega_2(t)\cup\Omega_3(t)} \tag{6}$$

where $\overline{\Omega}$ denotes the closure of the open set Ω. The boundary $\partial\Omega$ of Ω is decomposed in a similar manner into four disjoint subsets, Γ_{out}, Γ_{in}, Γ_w, and Γ_{axi}, as shown in Fig.9, such that

$$\partial\Omega = \overline{\Gamma_{out}\cup\Gamma_{in}\cup\Gamma_w\cup\Gamma_{axi}} \tag{7}$$

We denote by Γ_n and by Γ_c the interface between the nucleus and cytosol and the interface between the cytosol and the fluid, respectively. We denote by $\mathbf{n}$ and $\mathbf{t}$ the normal and tangential unit vectors

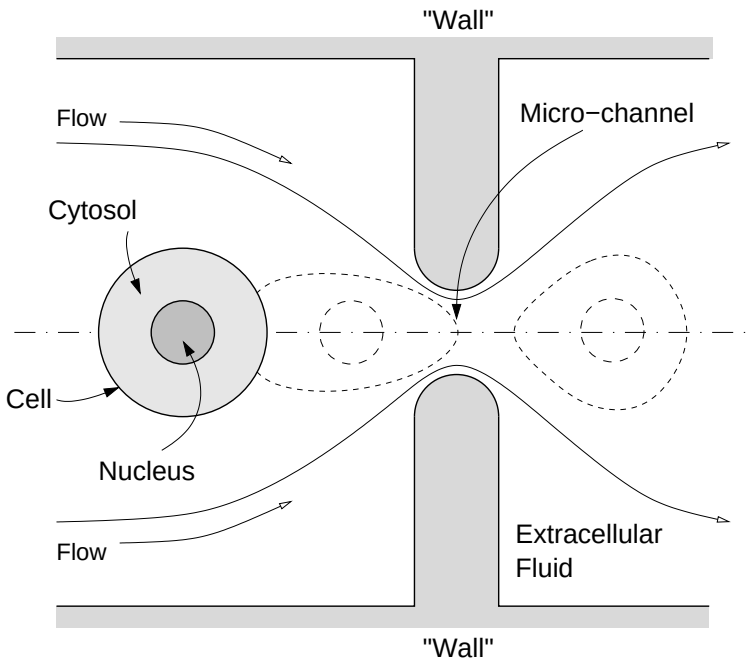

Figure 1: Schematic description of cell migration in a micro-channel.

associated with a boundary and we suppose that the dynamic viscosities of the nucleus, cytosol, and extracellular fluid are μ_1, μ_2, and μ_3, respectively.

The velocity $\mathbf{u}_1$ and pressure p_1 of the fluid in the nucleus are governed by the time-independent Stokes equations:

$$-\mu_1 \Delta \mathbf{u}_1 + \nabla p_1 = \mathbf{0} \qquad \text{in } \Omega_1(t) \tag{8}$$

$$\nabla \cdot \mathbf{u}_1 = 0 \qquad \text{in } \Omega_1(t) \tag{9}$$

while the flows in the cytosol and extracellular fluid are governed by:

$$-\mu_2 \Delta \mathbf{u}_2 + \nabla p_2 = \mathbf{0} \qquad \text{in } \Omega_2(t) \tag{10}$$

$$\nabla \cdot \mathbf{u}_2 = 0 \qquad \text{in } \Omega_2(t) \tag{11}$$

and

$$-\mu_3 \Delta \mathbf{u}_3 + \nabla p_3 = \mathbf{0} \qquad \text{in } \Omega_3(t) \tag{12}$$

$$\nabla \cdot \mathbf{u}_3 = 0 \qquad \text{in } \Omega_3(t) \tag{13}$$

These systems of equations are now supplemented with boundary conditions, interface conditions, and initial conditions.

2.2 Boundary Conditions

We assume that the extracellular matrix is rigid and immobile. Thus the domain Ω preserves its overall shape throughout the course of the simulation. Boundary conditions on $\partial\Omega$ (see Fig. 2) are

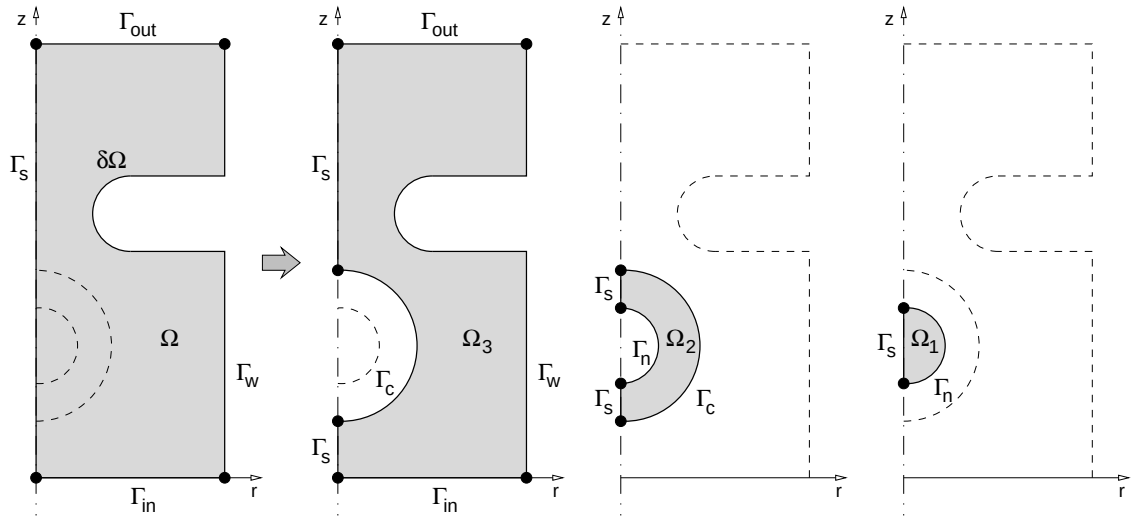

Figure 2: Decomposition of the computational domain Ω into subdomains Ω_1 (nucleus), Ω_2 (cytosol), and Ω_3 (extracellular fluid), and labeling of boundary and interface conditions (domain is not to scale).

prescribed as:

$$\text{No-slip BC:} \quad \mathbf{u}_3 = 0 \qquad \text{on } \Gamma_w \tag{14}$$

$$\text{Inflow BC:} \quad \mathbf{n}_3 \cdot \mu_3 \nabla \mathbf{u}_3 = \mathbf{0} \quad \text{and} \quad p_3 = p_{in} \qquad \text{on } \Gamma_{in} \tag{15}$$

$$\text{Outflow BC:} \quad \mathbf{n}_3 \cdot \mu_3 \nabla \mathbf{u}_3 = \mathbf{0} \quad \text{and} \quad p_3 = p_{out} \qquad \text{on } \Gamma_{out} \tag{16}$$

$$\text{Axisymmetry BC:} \quad \mathbf{n}_i \cdot \mathbf{u}_i = 0 \quad \text{and} \quad \mathbf{n}_i \cdot [-p_i \mathbf{I} + \mu_i \nabla \mathbf{u}_i] \cdot \mathbf{t}_i = 0, \;\; i = 1, 2, \text{ or } 3 \quad \text{on } \Gamma_{axi} \tag{17}$$

where $\mathbf{n}_i$ and $\mathbf{t}_i$ are the normal outward and tangent unit vectors with respect to Ω_i, respectively. We note that the motion of the cell is driven by the pressure gradient $\Delta p = p_{in} - p_{out}$ and that above conditions are all independent of time.

2.3 Interface Conditions between Cell Nucleus and Cytosol

The dynamic viscosity in the nucleus is assumed to be two to three orders of magnitude larger than that in the cytosol so that the nucleus is nearly non-deformable during cell migration. This assumption captures recent experimental results [13, 2, 11, 18, 12]. Moreover we imagine that the content of the nucleus is separated from the cytosol by a thin "membrane" or "nuclear envelope." In this case, the interface conditions are continuity of the velocity fields and continuity of stresses defined with respect to the surface of the interface Γ_n, that is,

$$\mathbf{u}_1 - \mathbf{u}_2 = \mathbf{0} \qquad \text{on } \Gamma_n(t) \tag{18}$$

$$\mathbf{n}_1 \cdot [-p_1 \mathbf{I} + \mu_1 \nabla \mathbf{u}_1] + \mathbf{n}_2 \cdot [-p_2 \mathbf{I} + \mu_2 \nabla \mathbf{u}_2] = \mathbf{0} \qquad \text{on } \Gamma_n(t) \tag{19}$$

where dependency in time is due to the moving interface Γ_n.

2.4 Interface Conditions between Cell and Extracellular Fluid

We suppose that the boundary of the cell is represented by a thin membrane that prevents fluid diffusion from one region to the other. The interface conditions should then be similar to the ones

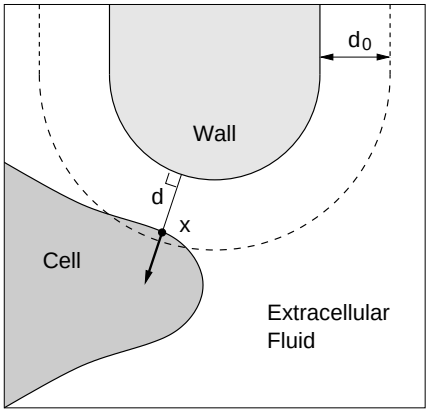

Figure 3: Schematic description of interaction model between cell surface and wall boundary.

prescribed in the previous section; i.e., continuity of the velocity fields and continuity of stresses. However, because the viscosities of the cytosol and of the extracellular fluid are assumed small and comparable, the cell membrane is flexible and results in surface tensions proportional to the mean curvature of the membrane κ with surface tension coefficient γ. Moreover, an additional constraint needs to be enforced at the surface of the cell; indeed, the cell cannot be allowed to come into contact with any of the wall boundaries as it would remain stuck to the wall otherwise. The constraint is modeled as follows: we imagine that there exists a repulsive pressure force between the cell and the wall whenever the cell approaches the wall within a user-defined distance, d_0 from the wall (see Fig. 3). Let $\mathbf{x}$ denotes a point on the cell surface Γ_c and let $d = d(\mathbf{x})$ denote the distance between $\mathbf{x}$ and the wall. Then the pressure governing the interaction between the cell and the wall is modeled as:

$$p_w(\mathbf{x}) = E_w\left(\frac{d(\mathbf{x})}{d_0} - 1\right) H\big(d_0 - d(\mathbf{x})\big), \qquad \forall \mathbf{x} \in \Gamma_c \tag{20}$$

where H is the Heaviside step function and E_w is a spring constant. Such a boundary condition intends to mimic a slip-boundary condition along the wall, with slippage controlled by the parameter d_0. This model for pressure p_w is defined in terms of the two parameters E_w and d_0 that will be carefully chosen in order to obtain reasonable results.

The interface conditions on Γ_c are then prescribed as:

$$\mathbf{u}_2 - \mathbf{u}_3 = \mathbf{0} \qquad \text{on } \Gamma_c(t) \tag{21}$$

$$\mathbf{n}_2 \cdot [-p_2\mathbf{I} + \mu_2 \nabla \mathbf{u}_2] + \mathbf{n}_3 \cdot [-p_3\mathbf{I} + \mu_3 \nabla \mathbf{u}_3] - \mathbf{n}_2 \cdot [-p_w\mathbf{I} + \gamma\kappa\mathbf{I}] = \mathbf{0} \qquad \text{on } \Gamma_c(t) \tag{22}$$

where the surface tension coefficient γ is assumed uniform along the cell surface and time-independent.

2.5 Time Evolution

At the initial time t_0, we suppose that the cell is spherical and that its centroid is located on the axis of symmetry. The time interval $(0, T)$ can be divided into uniform subintervals (t_{j-1}, t_j), $j = 1, 2, \ldots, N$, with constant time step $\Delta t = T/N$.

Let us suppose that the domains Ω_1, Ω_2, and Ω_3 are known at time t_{j-1}, where $j = 1, 2, \ldots,$ or N. In order to update the cell geometry within the extracellular fluid from time t_{j-1} to time t_j, we

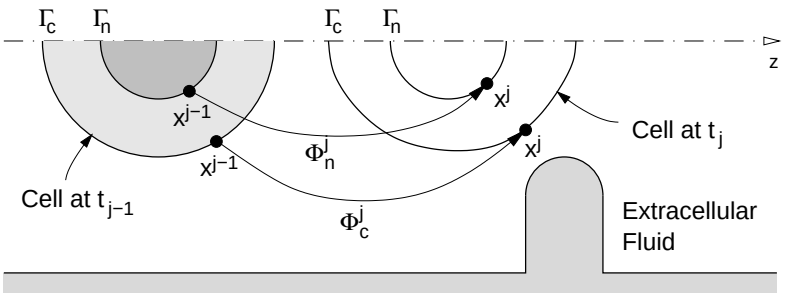

Figure 4: Definition of the mappings Φ_n^j and Φ_c^j for the time evolution.

solve the coupled system of equations presented above for the velocity fields $\mathbf{u}_1(t_{j-1})$, $\mathbf{u}_2(t_{j-1})$, and $\mathbf{u}_3(t_{j-1})$ on $\Omega_1(t_{j-1})$, $\Omega_2(t_{j-1})$, $\Omega_3(t_{j-1})$, respectively. The domains are then updated by mapping the interfaces Γ_n and Γ_c from time t_{j-1} to time t_j, $j = 1, \ldots, N$, as follows:

$$\begin{aligned}
&\Phi_n^j : \Gamma_n(t_{j-1}) \to \Gamma_n(t_j) \\
&\qquad \mathbf{x}^{j-1} \to \mathbf{x}^j = \mathbf{x}^{j-1} + \Delta t\ \mathbf{u}_1(\mathbf{x}^{j-1}, t_{j-1}), \qquad \forall \mathbf{x}^{j-1} \in \Gamma_n(t_{j-1}) \qquad (23)\\
&\Phi_c^j\ : \Gamma_c\,(t_{j-1}) \to \Gamma_c\,(t_j) \\
&\qquad \mathbf{x}^{j-1} \to \mathbf{x}^j = \mathbf{x}^{j-1} + \Delta t\ \mathbf{u}_2(\mathbf{x}^{j-1}, t_{j-1}), \qquad \forall \mathbf{x}^{j-1} \in \Gamma_c\,(t_{j-1}) \qquad (24)
\end{aligned}$$

where the transformations (23) and (24) simply correspond to the discretization of the time differential equation $\mathbf{u} = d\mathbf{x}/dt$. Migration of the cell is thus approximated by a discrete quasi-static process that depends on the discretization parameter Δt. This process is illustrated in Fig. 4.

3 Finite Element Discretization of coupled problem

3.1 Weak Formulation

We first derive the weak formulation of the Stokes problems in Ω_i, $i = 1, 2, 3$:

$$-\mu_i \Delta \mathbf{u}_i + \nabla p_i = \mathbf{0} \qquad \text{in } \Omega_i = \Omega_i(t) \qquad (25)$$

$$\nabla \cdot \mathbf{u}_i = 0 \qquad \text{in } \Omega_i = \Omega_i(t) \qquad (26)$$

subjected to the boundary and interface conditions described above. The weak form of the equations is obtained by multiplying the momentum equation (25) and continuity equation (26) by smooth test functions $\mathbf{v}_i$ and q_i, integrating over the whole domain Ω_i, integrating by parts, and applying the divergence theorem. We thus have:

$$\int_{\Omega_i} \mu_i \nabla \mathbf{u}_i : \nabla \mathbf{v}_i \, dx - \int_{\Omega_i} p_i \nabla \cdot \mathbf{v}_i \, dx + \int_{\partial \Omega_i} \mathbf{n}_i \cdot [-p_i \mathbf{I} + \mu_i \nabla \mathbf{u}_i] \cdot \mathbf{v}_i \, ds = 0, \quad \forall \mathbf{v}_i \text{ smooth} \qquad (27)$$

$$-\int_{\Omega_i} q_i \nabla \cdot u_i \, dx = 0, \quad \forall q_i \text{ smooth} \qquad (28)$$

We now apply the boundary conditions for each of the domain. We first note that the boundary contributions defined on the axisymmetric boundary necessarily vanish since $r = 0$. We then have:

$$\int_{\Omega_1} \mu_1 \nabla \mathbf{u}_1 : \nabla \mathbf{v}_1 \, dx - \int_{\Omega_1} p_1 \nabla \cdot \mathbf{v}_1 \, dx + \int_{\Gamma_n} \mathbf{n}_1 \cdot [-p_1 \mathbf{I} + \mu_1 \nabla \mathbf{u}_1] \cdot \mathbf{v}_1 \, ds = 0, \quad \forall \mathbf{v}_1 \tag{29}$$

$$- \int_{\Omega_1} q_1 \nabla \cdot u_1 \, dx = 0, \quad \forall \, q_1 \tag{30}$$

$$\int_{\Omega_2} \mu_2 \nabla \mathbf{u}_2 : \nabla \mathbf{v}_2 \, dx - \int_{\Omega_2} p_2 \nabla \cdot \mathbf{v}_2 \, dx + \int_{\Gamma_n} \mathbf{n}_2 \cdot [-p_2 \mathbf{I} + \mu_2 \nabla \mathbf{u}_2] \cdot \mathbf{v}_2 \, ds$$
$$+ \int_{\Gamma_c} \mathbf{n}_2 \cdot [-p_2 \mathbf{I} + \mu_2 \nabla \mathbf{u}_2] \cdot \mathbf{v}_2 \, ds = 0 \quad \forall \mathbf{v}_2 \tag{31}$$

$$- \int_{\Omega_2} q_2 \nabla \cdot u_2 \, dx = 0, \quad \forall \, q_2 \tag{32}$$

$$\int_{\Omega_3} \mu_3 \nabla \mathbf{u}_3 : \nabla \mathbf{v}_3 \, dx - \int_{\Omega_3} p_3 \nabla \cdot \mathbf{v}_3 \, dx + \int_{\Gamma_c} \mathbf{n}_3 \cdot [-p_3 \mathbf{I} + \mu_3 \nabla \mathbf{u}_3] \cdot \mathbf{v}_3 \, ds$$
$$- \int_{\Gamma_{in}} p_{in} \, \mathbf{n}_3 \cdot \mathbf{v}_3 \, ds - \int_{\Gamma_{out}} p_{out} \, \mathbf{n}_3 \cdot \mathbf{v}_3 \, ds = 0, \quad \forall \mathbf{v}_3 \tag{33}$$

$$- \int_{\Omega_2} q_3 \nabla \cdot u_3 \, dx = 0, \quad \forall \, q_3 \tag{34}$$

where the test functions $\mathbf{v}_3$ are chosen to vanish on the boundary Γ_w. Summing up the momentum equations and continuity equations above, applying the interface conditions on Γ_n and Γ_c, introducing $\mu = \mu(\mathbf{x})$ such that $\mu = \mu_1$ on Ω_1, $\mu = \mu_2$ on Ω_2, and $\mu = \mu_3$ on Ω_3, introducing $(\mathbf{u}, p)$ and $(\mathbf{v}, q)$ defined in a similar manner in terms of $(\mathbf{u}_1, p_1)$, $(\mathbf{u}_2, p_2)$, $(\mathbf{u}_3, p_3)$, and $(\mathbf{v}_1, q_1)$, $(\mathbf{v}_2, q_2)$, $(\mathbf{v}_3, q_3)$, respectively, observing that the velocity fields $\mathbf{u}_1$ and $\mathbf{u}_2$ and $\mathbf{u}_2$ and $\mathbf{u}_3$ are continuous at the interfaces Γ_n and Γ_c, and finally, introducing the spaces of trial and test functions V and Q such as:

$$V = \left\{ \mathbf{v} \in (H^1(\Omega))^2; \ \mathbf{v} = \mathbf{0}, \text{ on } \Gamma_w \right\} \tag{35}$$

$$Q = \left\{ q \in L^2(\Omega); \ \int_\Omega q \, dx = 0 \right\} \tag{36}$$

the weak form of our coupled problem can be recast in the simple form:

Find $(\mathbf{u}, p) \in V \times Q$ such that

$$\int_\Omega \mu \nabla \mathbf{u} : \nabla \mathbf{v} \, dx - \int_\Omega p \ \nabla \cdot \mathbf{v} \, dx = \int_{\Gamma_c} (-p_w + \gamma \kappa) \mathbf{n} \cdot \mathbf{v} \, dx$$
$$+ \int_{\Gamma_{in}} p_{in} \, \mathbf{n} \cdot \mathbf{v} \, ds + \int_{\Gamma_{out}} p_{out} \, \mathbf{n} \cdot \mathbf{v} \, ds, \quad \forall \mathbf{v} \in V \tag{37}$$
$$- \int_\Omega q \ \nabla \cdot u \, dx = 0, \quad \forall \, q \in Q$$

where the normal vector $\mathbf{n}$ on Γ_c is chosen as $\mathbf{n}_2$. The above Stokes problem is a classical symmetric mixed problem for which existence and uniqueness of solutions have long been established [9].

3.2 Finite Element formulation

The domain Ω is first discretized into a triangulation $\mathcal{T}_h$ made of triangular elements K_e, $e = 1, \ldots, N_e$, N_e being the total number of elements, in such a way that the interfaces Γ_n and Γ_c are

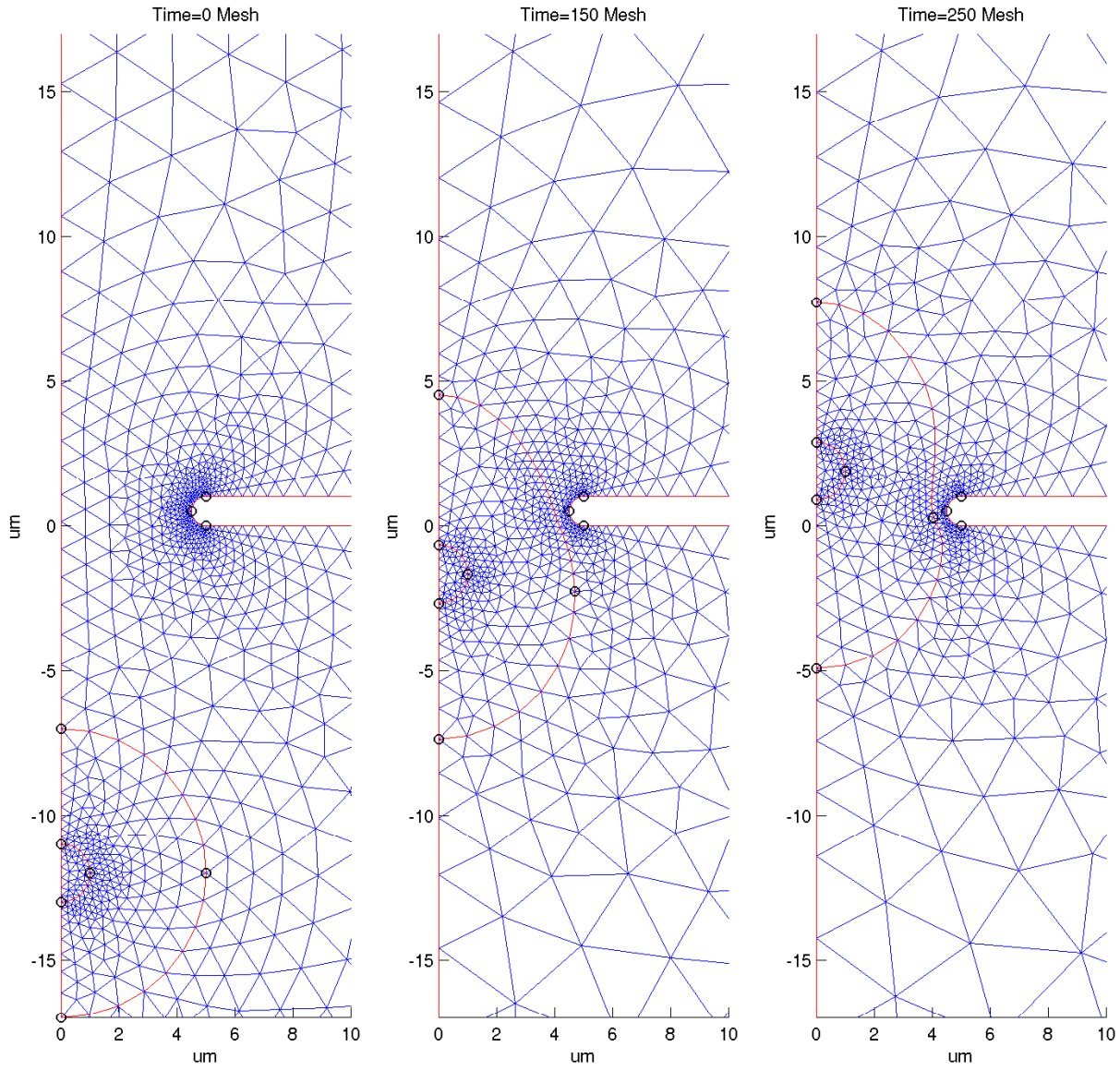

Figure 5: Example of initial unstructured mesh and corresponding meshes at times $t = 150$ s and $t = 250$ s. The profiles of the nucleus and cell are shown in red.

approximated as Γ_n^h and Γ_c^n, respectively, as shown in Fig. 5. We define the computational domain as $\Omega_h = \cup_e K_e$ and observe that the wall boundary is discretized into a new boundary Γ_w^h due to its curvilinear shape. At each time step, the domain Ω^h is updated by simply re-meshing the new geometry based on the solution of the Stokes problem at the previous instant of time. We define the finite element subspaces V^h and Q^h of V and Q, respectively, as:

$$V^h = \left\{ \mathbf{v}_h \in (C_0(\Omega^h))^2;\ \mathbf{v}_h|_{K_e} \in (\mathbb{P}_2)^2,\ \forall K_e \in \mathcal{T}_h;\ \mathbf{v}_h = \mathbf{0},\ \text{on } \Gamma_w^h \right\} \tag{38}$$

$$Q^h = \left\{ q_h \in C_0(\Omega^h);\ q_h|_{K_e} \in \mathbb{P}_1,\ \forall K_e \in \mathcal{T}_h;\ \int_{\Omega^h} q_h\, dx = 0 \right\} \tag{39}$$

where $\mathbb{P}_k$ denotes the space of polynomials of degree k, $k = 1$, 2, and $C_0(\Omega^h)$ the set of continuous functions on Ω^h. This choice of finite element spaces ensures that the discrete finite element problem defined below actually satisfied the inf-sup condition. The finite element problem corresponding to (37) then reads:

Find $(\mathbf{u}_h, p_h) \in V^h \times Q^h$ such that

$$\begin{aligned} \int_{\Omega^h} \mu \nabla \mathbf{u}_h : \nabla \mathbf{v}_h\, dx - \int_{\Omega^h} p_h\ \nabla \cdot \mathbf{v}_h\, dx &= \int_{\Gamma_c^h} (-p_w + \gamma \kappa_h) \mathbf{n} \cdot \mathbf{v}_h\, dx \\ &+ \int_{\Gamma_{in}} p_{in}\ \mathbf{n} \cdot \mathbf{v}_h\, ds + \int_{\Gamma_{out}} p_{out}\ \mathbf{n} \cdot \mathbf{v}_h\, ds, \quad \forall \mathbf{v}_h \in V^h \\ - \int_{\Omega^h} q_h\ \nabla \cdot u_h\, dx &= 0, \quad \forall\, q_h \in Q^h \end{aligned} \tag{40}$$

where κ_h is the mean curvature of the interface Γ_c^h. A priori error estimates show that the finite element solution $(\mathbf{u}_h, p_h)$ of (40) converges to the solution $(\mathbf{u}, p)$ of (37) as the mesh is refined, i.e. as the mesh size h tends to zero [9].

3.3 Numerical Algorithm

The finite element application of the cell migration problem was implemented in the commercial COMSOL Multiphysics using the "fluid dynamics" option and the "mesh-deformation" option. The numerical algorithm for one simulation of the problem can be described as follows:

1. Generate the initial mesh Ω_0^h.
2. For $j = 1, \ldots, N$
   (a) Solve the steady-state Finite Element problem (40) for the velocity field $\mathbf{u}_h^{j-1}$ and pressure p_h^{j-1} in the whole domain Ω_{j-1}^h;
   (b) Given the velocity field inside the cell, compute the deformation of the cell using the mesh-deformation solver;
   (c) Map the updated geometry of the cell back to the initial configuration.
   (d) Generate the new mesh Ω_j^h.
   (e) If $j < N$, go to Step 2.
3. End.

4 Numerical Experiments

We now present numerical experiments for the simulation of cell migration through micro-channels. We shall in particular make a parameter study in which the hole diameter, the surface tension of the cell membrane, and the viscosity of the cytosol are varied.

4.1 Numerical Setting

4.1.1 Input Parameters

Table 1 collects the list of input modeling parameters used in the following numerical experiments. We model a typical cell with diameter $D_c = 10$ μm containing a nucleus with diameter D_n varying between 0.0 μm (no nucleus) and 7.0 μm. The cell is considered as a liquid droplet consisting of cell membrane, cytosol, and nucleus. Here, the existence of cytoskeletal network and other important organelles in the cytosol is ignored. The cell migrates through a micro-channel of length $L_h = 1$ μm and diameter D_h varying within the range 5.0 μm to 15 μm. The wall of the channel has a semi-circular shape so that the flow is smoother than in the case of a rectangular shape. The overall dimensions of the computational domain are chosen sufficiently large in order to minimize boundary effects as we are primarily interested in the flow in the vicinity of the channel. The pressure gradient Δp from one end of the domain to the other end is set so that the entire course of migration takes minutes to tens of minutes. The extracellular fluid is assumed to be water. Since the nucleus is supposed to be non-deformable, we choose its viscosity to be of at least three orders of magnitude larger than that of the cytosol. The surface tension γ of the cell is arbitrarily chosen but it cannot be too large as otherwise the cell could not be able to migrate through the channel. The gap d_0 between the cell surface and wall is also arbitrarily chosen, as well as the spring constant E_w associated with the wall, but the latter needs to be sufficiently large in order to overcome the total pressure from the cell. These parameters could alternatively be calibrated using some experimental data; we chose not to in this study as we are more interested in the comparison of the behavior of the cell as other parameters are varied (e.g. the diameter of the nucleus D_n, the diameter of the channel/hole D_h, and the surface tension γ).

4.1.2 Output Quantities

For comparison purposes, we now introduce some relevant quantities of interest. The solution of the problem consists in the velocity and pressure fields in the whole domain and for the whole time interval (assuming that the fields vary linearly within each time subinterval). We can then post-process the solution to compute the longitudinal displacement at the top, bottom, and centroid of the cell as well as at the centroid of the nucleus. We shall denote these displacements by z_t, z_b, z_c, and z_n, respectively. Using the displacement z_c of the centroid of the cell, we also introduce the discrete velocity along the axis at each time step calculated as:

$$u_c(t_j) = \frac{z_c(t_{j+1}) - z_c(t_j)}{\Delta t}, \qquad j = 0, \ldots, N-1 \tag{41}$$

Note that z_c is easily obtained from the geometry of the cell at each time step. The quantity of interest is defined as the "average velocity" of the cell with respect to the time that the cell spends in the channel. The period during which the cell is "in the channel" is defined as the difference between the time t_{out} at which the bottom of the cell exits the channel and the time t_{in} at which the top of the cell enters the channel. We denote by N_{out} and N_{in} the iteration indices corresponding

Table 1: Parameters used in the numerical simulations of the cell migration process.

Parameters	Symbols	Units	Values
Initial cell diameter	D_c	μm	10.0
Initial nucleus diameter	D_n	μm	0.0 – 7.0
Hole length	L_h	μm	1.0
Hole diameter	D_h	μm	5.0 – 15.0
Domain diameter	D_d	μm	80.0
Domain length	L_d	μm	120.0
Gap between cell surface and wall	d_0	μm	0.5
Viscosity of nucleus	μ_1	mPa $\cdot$ s	20000.0
Viscosity of cytosol	μ_2	mPa $\cdot$ s	20.0
Viscosity of extracellular fluid	μ_3	mPa $\cdot$ s	0.894
Pressure gradient	Δp	mPa	0.5
Spring constant of wall	E_w	mPa	50.0
Surface tension	γ	μPa $\cdot$ m	0.0 – 0.005

to t_{out} and t_{in} respectively. The output quantity of interest is then defined as:

$$\bar{v}_c = \frac{1}{N_{out} - N_{in}} \sum_{j=N_{in}}^{N_{out}} u_c(t_j) \tag{42}$$

We note here that $\bar{v}_c$ is actually an approximation of the true averaged velocity due to the discretization parameters h and Δt. We verify below that the computed average velocity is nevertheless accurate with respect to these two parameters.

4.1.3 Verification Tests

Verification tests are first run using different mesh sizes and time steps in order to assess the accuracy of the numerical solutions for a given set of input parameters. The displacements of the cell over time as well as the average velocity $\bar{v}_c$ were compared. To verify the convergence of the solution with respect to the mesh size, we considered along the mesh of reference a coarser mesh and a finer mesh as shown in Fig. 6. The simulations with coarser and finer meshes yield virtually the same results (see Fig. 7). Simulation with a larger time step and a smaller time step were also performed and yield very similar results once again, as shown in Fig. 8. Actually, for both comparisons, the difference in the displacement z_c of the cell at each time step is smaller than one percent. We are thus confident that the mesh size and time step are chosen small enough for the solutions to be converged.

4.2 Description of the Dynamics of Migration

The entire course of a typical migration is illustrated in Fig. 9. One should note that the cell dynamically changes its shape to crawl through the channel, where it exhibits a contractile ring formation and vertical elongation. It deforms back to circular shape upon exiting the channel and the time taken to recover its initial shape directly depends on the pressure gradient Δp and the strength of the surface tension coefficient γ. These sequence of events are qualitatively very similar to the experimental studies by Friedl and co-workers [4], [5]. We observe that the cell nucleus

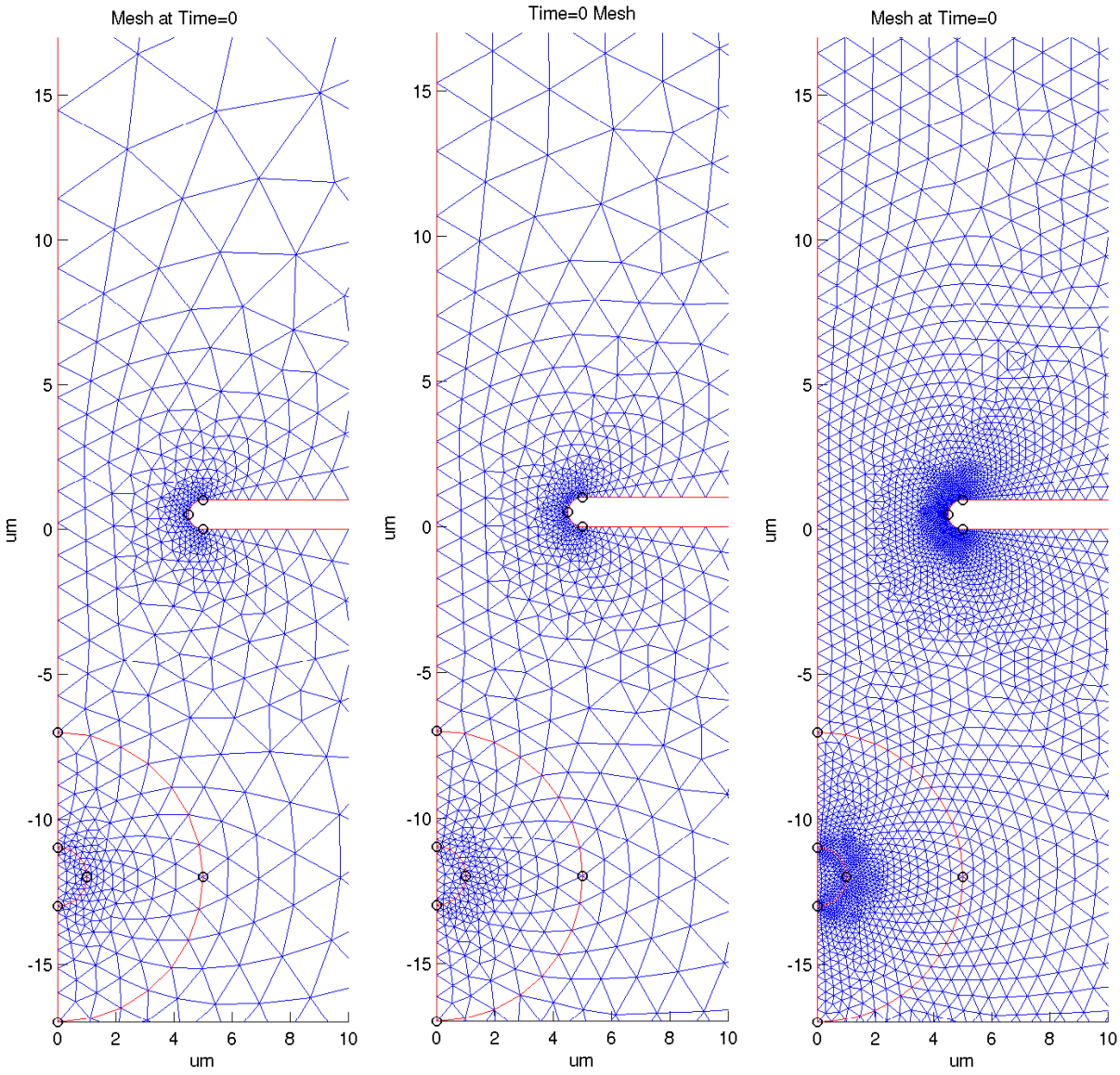

Figure 6: Reference mesh (center) along with coarser mesh (left) and finer mesh (right).

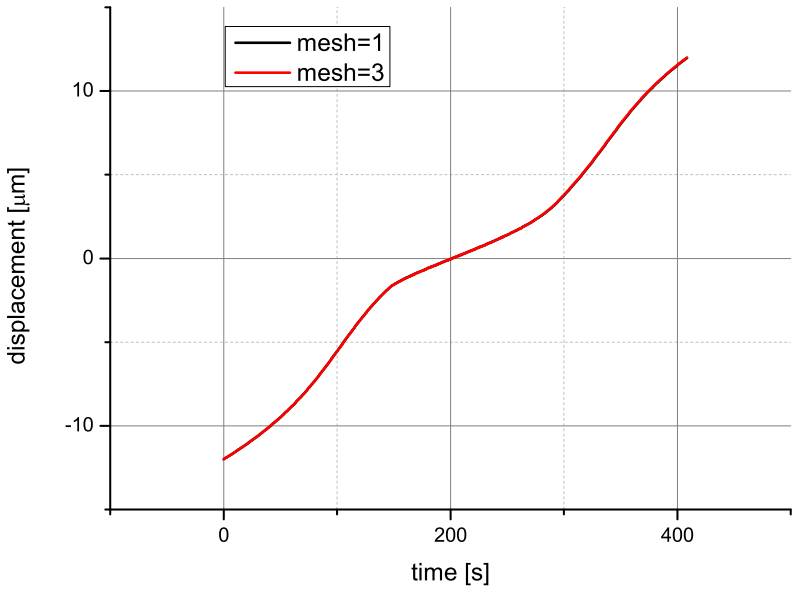

Figure 7: Evolution in time of displacement z_c of a cell migrating through a channel with $D_h = 10$ μm for different meshes.

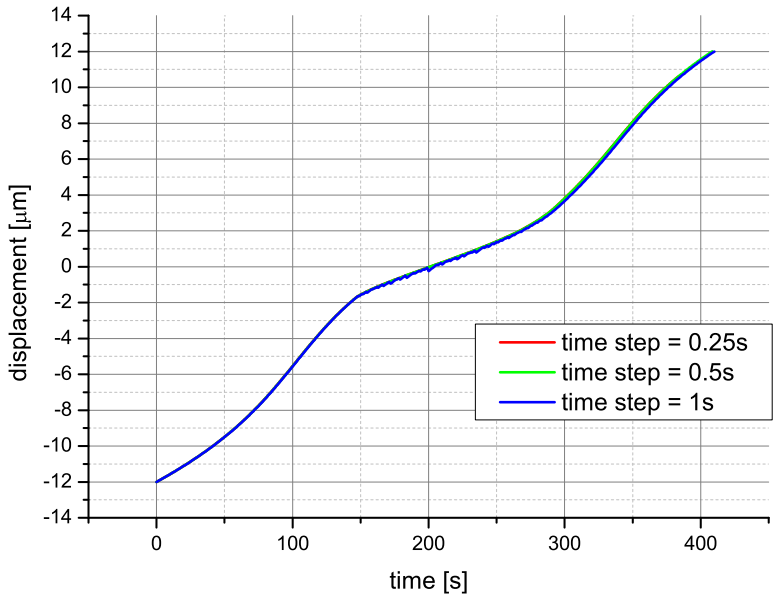

Figure 8: Evolution in time of displacement z_c of a cell migrating through a channel with $D_h = 10$ μm for three different values of the time step Δt.

does not deform during the simulation, as expected, and essentially remains at the center of the cell, as observed in 3D amoeboid cell migration experiments. The gap between the cell membrane and the wall is of course introduced by the interfacial pressure model introduced earlier. The time evolutions of the displacements z_t, z_b, and z_c for the cell, and z_n for the nucleus are shown in Fig. 10 and Fig. 11, respectively. In these experiments, the diameter of the nucleus D_n and surface tension coefficient γ are set constant. However, in Fig. 10, the diameter of the channel is set to $D_h = 10$ μm whereas it is set to 8 μm for the simulation of Fig. 11. It is clear that a cell takes a much longer time to crawl through a smaller channel. While the cell is in the hole, vertical elongation of the cell can be observed. The smaller the hole, the longer the cell elongates due to the incompressibility assumption. Also, we can verify that the nucleus does not necessarily move together with the centroid of the cell. When a cell crawls through a relatively small hole, the centroid of the nucleus exits the channel ahead of the centroid of the cell and the position of the two centroids coincide again after a certain period of time. This is particularly interesting since the nuclear dynamics have not been fully quantified in experimental studies. We believe that our simulations provide a first of its kind look on the internal dynamics of the cell that will improve our understanding of cytoskeletal reorganization in 3D cell motion. The velocity u_c with respect to time is illustrated in Fig. 12. It is noticeable that the velocity of the centroid reaches a local maximum right before and right after the cell moves in and out of the channel. Between these two peaks, the cell experiences low and relatively constant velocities. The cell is accelerated before entering and after exiting the channel because of sudden pressure changes in these regions. The low and relatively constant velocity of the cell inside the channel is observed because of large viscosity coefficients inside the cell as compared to the one outside and because of the slow fluid motion between the cell membrane and matrix wall, which drives the cell forward. These behaviors of the cell velocity are characteristic in the dynamics of cell migration. They can be observed in actual laboratory experiments and were also observed by Dembo while using a micropipet aspiration model [3].

4.3 Numerical Studies and Parameter Sensitivities

4.3.1 Effect of channel diameter

Figure 13 shows the average velocity of the cell in the channel with respect to the diameter of the channel. The diameter of the cell is set to $D_c = 10$ μm and the diameter of the nucleus is taken as $D_n = 2$ μm. Thus the cell needs to elongate in order to migrate through the channel. We observe that the velocity approaches zero as the diameter of the channel D_h is decreased. However, the velocity of the cell reaches zero for a critical value of D_h due to surface tension and the fact that the nucleus is non-deformable. Indeed, the cell asymptotically reaches a static equilibrium while it migrates through the channel as soon as the surface tension is greater than a "critical surface tension" or when the width of the channel is smaller than the diameter of the nucleus. This critical surface tension depends on the channel diameter and pressure gradient. When the channel is smaller than the initial cell radius, the velocity of the cell follows an exponential behavior. In contrast, when the channel diameter is larger, the velocity of the cell has a linear behavior because the interactions between the cell membrane and the wall become negligible.

4.3.2 Effect of surface tension

Figure 14 shows the average velocity $\bar{v}_c$ of the cell with respect to different values of the surface tension γ when the channel diameter is smaller than the cell diameter. These curves exhibit a similar behavior when the channel diameter is sufficiently large and the velocity tends to zero as channel diameter is decreased. Unfortunately, it becomes very difficult to exactly evaluate the

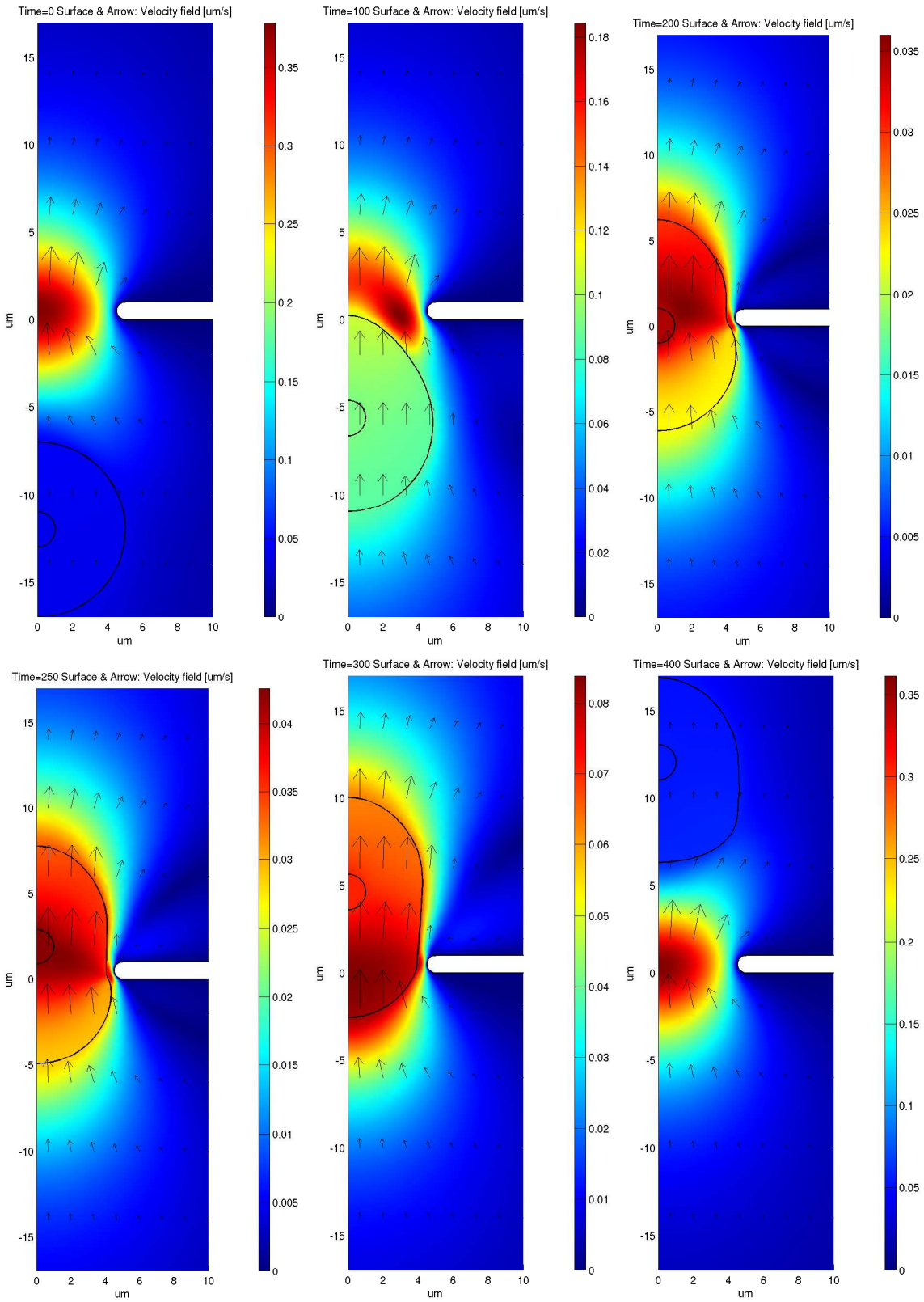

Figure 9: Snapshots of the process of cell migration through a small channel. Arrows and colors represent the distribution of the velocity vector and velocity magnitude of the flow.

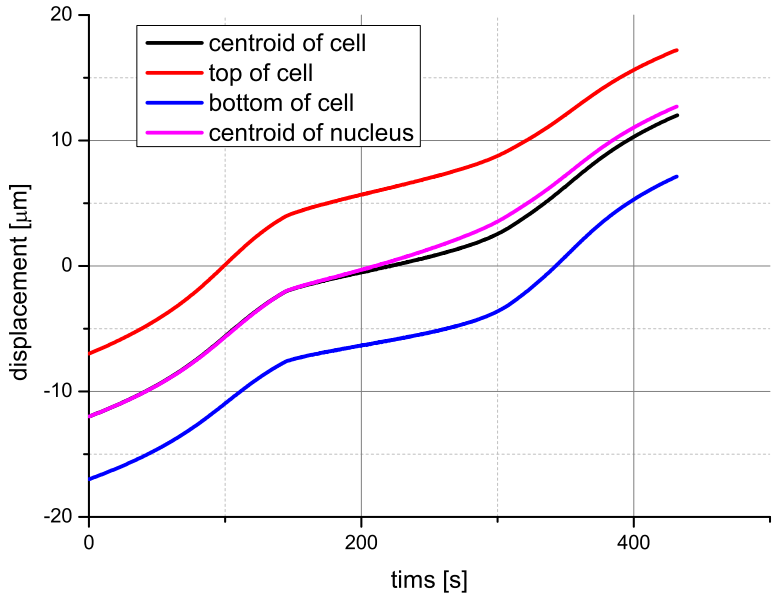

Figure 10: Time evolution of approximated displacements z_c, z_t, z_b, and z_n for a cell migrating through a channel with $D_h = 10$ μm.

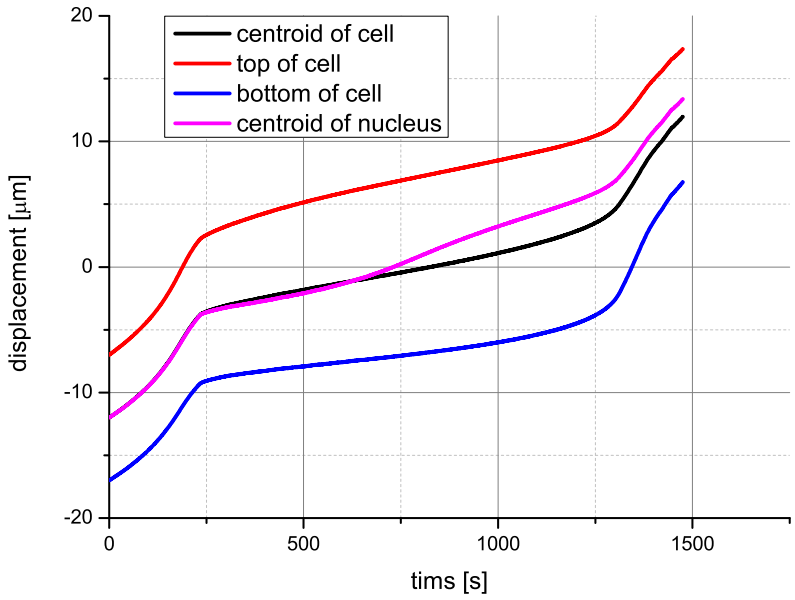

Figure 11: Time evolution of approximated displacements z_c, z_t, z_b, and z_n for a cell migrating through a channel with $D_h = 8$ μm.

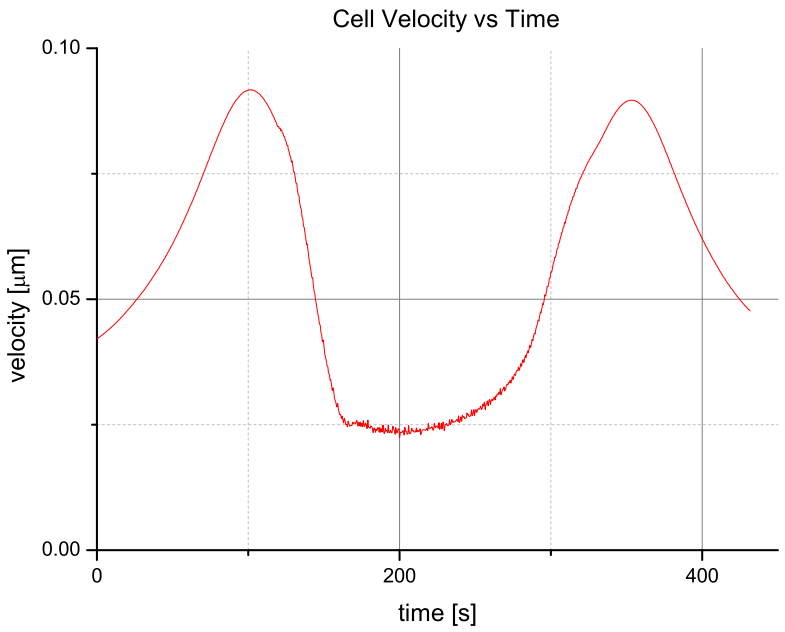

Figure 12: Time evolution of computed velocity u_c of the cell.

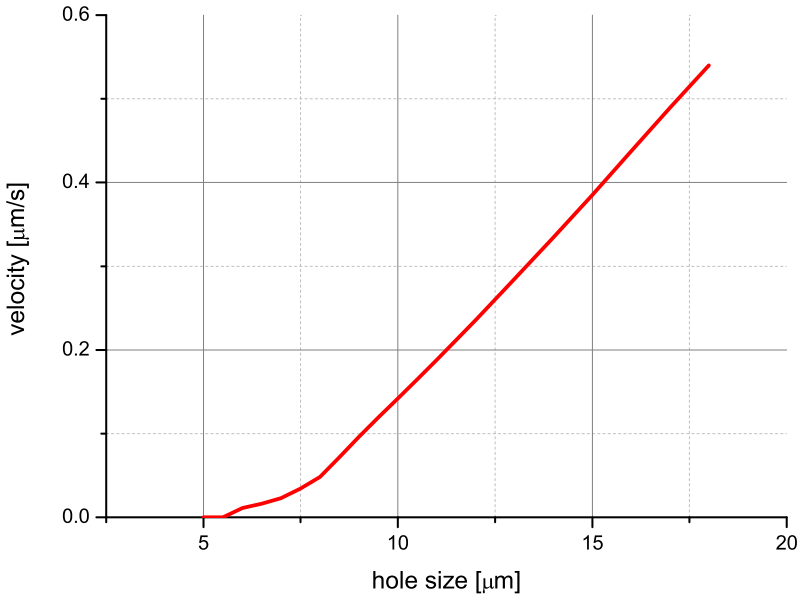

Figure 13: Average velocity $\bar{v}_c$ of the cell versus channel diameter D_h.

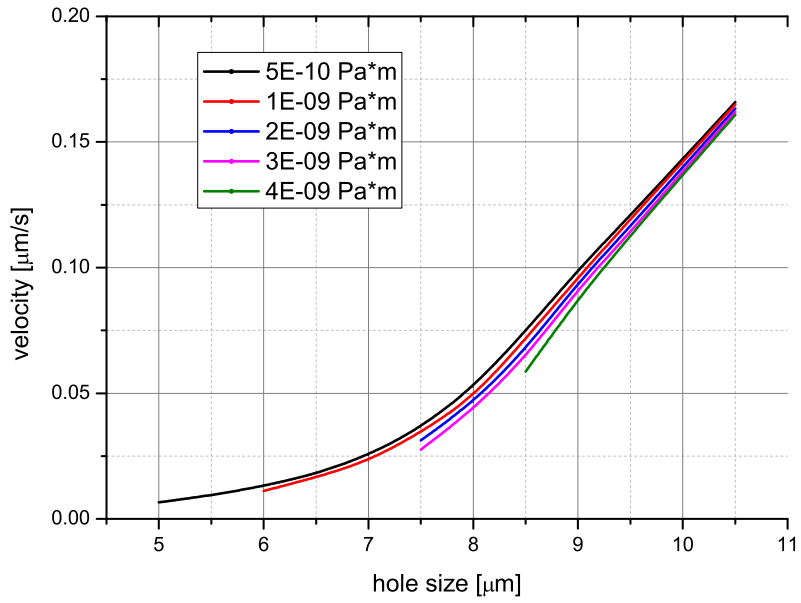

Figure 14: Average velocity $\bar{v}_c$ of the cell versus channel diameter D_h for different values of the surface tension γ.

critical channel diameter at which $\bar{v}_c$ vanishes as it would require infinitely long simulations. For large values of the channel diameter, the average velocities are nevertheless similar independently of the surface tension since the cell deforms into very similar shapes when it migrates through the channel. We also observe that when the surface tension γ becomes larger, $\bar{v}_c$ slightly decreases; this can be explained by the fact that, in that case, the cell membrane moves closer to the walls of the channel where the flow motion is necessarily slower. Therefore, the average velocity of the cell is directly related to the distance d between the cell surface and the channel walls. The cell is actually maintained at a constant distance d throughout the migration because the total pressure from outside corresponds with the total pressure from inside. This distance could nevertheless be modified by considering different values of d_0 and E_w in our model. Below a certain diameter of the channel, the cell reaches a static equilibrium whenever the surface tension γ becomes larger than a "critical surface tension" γ_{crit} as the force driven by the pressure gradient, Δp, cannot overcome the surface tension force. The velocity of the cell should then rapidly drop right at this critical surface tension.

When the cell reaches static equilibrium, we assume that the cell and wall decompose the whole domain Ω into three: the region represented by the flow downstream of the cell, Ω_{ds}, the domain upstream of the cell, Ω_{us}, and the region occupied by the cell, Ω_c (see Fig. 15). At equilibrium, the velocity of the cell as well as of the extracellular fluid vanishes. Therefore, from the continuity and momentum equations, the pressure in these three domains should be constant. Let us denote the boundary between Ω_{us} and Ω_c as Γ_{uc}, the boundary between Ω_{ds} and Ω_c as Γ_{dc}, and the one shared by the wall and the cell as Γ_{wc}. Using the boundary conditions between the cell and extracellular fluid, we derive the following relation:

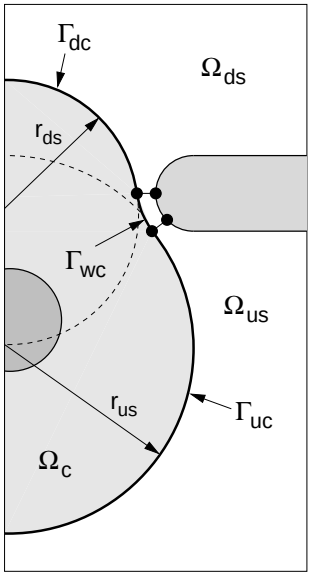

Figure 15: Description of the cell in equilibrium configuration for theoretical modeling of the critical surface tension.

$$P_{ds} - P_c = \kappa_{dc}\gamma, \quad \text{on } \Gamma_{dc} \tag{43}$$

$$P_{us} - P_c = \kappa_{uc}\gamma, \quad \text{on } \Gamma_{uc} \tag{44}$$

where P_{us}, P_{ds}, and P_c are the equilibrium pressures in Ω_{us}, Ω_{ds}, and Ω_c, respectively, and κ_{dc} and κ_{uc} are the curvatures of the boundaries Γ_{dc} and Γ_{uc}, respectively. Because the cell is in equilibrium, Γ_{dc} and Γ_{uc} should be spherical, and thus κ_{dc} and κ_{uc} should be constant over these boundaries. Therefore, we can derive the expression,

$$P_{ds} - P_{us} = \Delta p = (\kappa_{dc} - \kappa_{uc})\gamma \tag{45}$$

We can determine the shape of the cell at equilibrium from its initial radius and shape of the channel. We could thus calculate the radii r_{ds} and r_{us} of the semicircles downstream and upstream of the cell. Since the curvature of a circle is the inverse of its radius, we can derive the "critical surface tension" of the cell, which defines the minimum value of the surface tension at which equilibrium occurs, i.e. at which the cell gets "stuck" in the channel,

$$\gamma_{crit} = \frac{\Delta p}{1/r_{ds} - 1/r_{us}}. \tag{46}$$

This critical surface tension is actually an approximation of the actual one as we do not take into account in the present analysis the gap between the cell membrane and matrix wall where there is actually a flow. We also ignore here the part of the cell boundary, Γ_{wc}. Thus, the smaller the prescribed value of the gap d_0 is, the better the approximation should be.

Figure 16 shows the critical surface tension computed by the theory described above and numerical values. Note that the critical surface tension reaches infinite as the hole width exceeds the initial diameter of the cell. The computed critical surface tensions take a range because it is

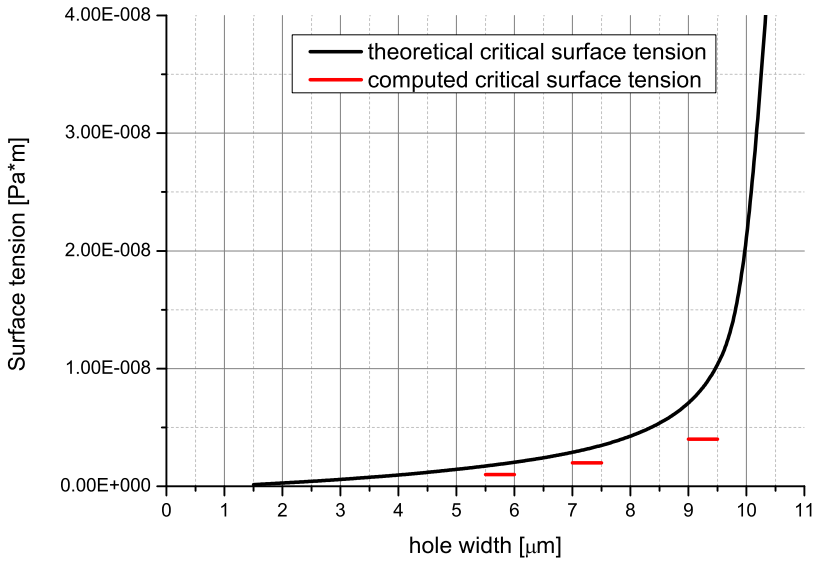

Figure 16: Comparison of theoretical and numerical critical surface tension with respect to the diameter D_h of the micro-channel.

impossible to calculate the minimum surface tension at which the cell reaches equilibrium. The computed values are always below the theoretical value. The discrepancy mainly comes from the fact that it is hard to determine whether the cell is at equilibrium or moving extremely slowly. Also, near the equilibrium, the simulation becomes unstable, prone to numerical errors. Thus the numerical computation always underestimates the value. Other than that, the theory estimates the critical surface tension very accurately. Finally, note that the diameter of the nucleus does no effect on the critical surface tension unless it exceeds the hole width.

4.3.3 Effect of Nucleus Size

Figure 17 shows the average velocity $\bar{v}_c$ of the cell with respect to different nucleus diameters. Each curve is obtained for a different channel diameter. Because the nucleus is assumed non-deformable and is constrained to be contained within the cell, its diameter cannot exceed the smallest dimension of the cell nor the channel diameter. The figure shows that the larger the nuclear diameter, the smaller the average velocity of the cell. In other words, the cell becomes more "viscous" as a whole and thus moves slower. The discussion about the critical surface tension demonstrates that the dimension of the nucleus does not affect the critical surface tension unless the size of the nucleus exceeds the size of the channel. If the surface tension is smaller than the critical surface tension and the size of the channel, the cell should be able to go through the channel. Therefore, the curve showing the average velocity $\bar{v}_c$ with respect to the size of the nucleus is discontinuous at the critical nucleus diameter, which is just the size of the hole. If the size of the nucleus exceeds the critical nuclear size, the average velocity should inevitably become zero.

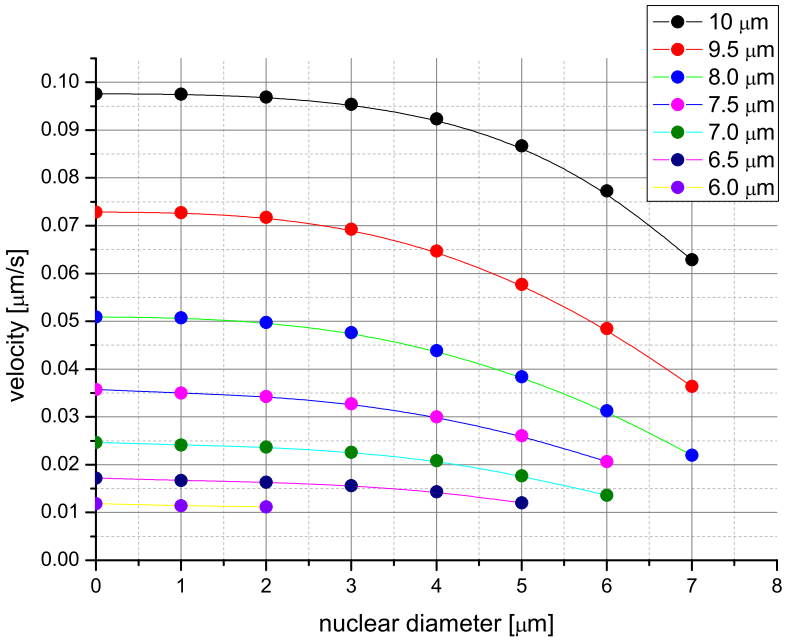

Figure 17: Average velocity $\bar{v}_c$ versus the diameter D_n of the nucleus for different values of the channel diameter D_h.

5 Conclusions

While our simulation provides a first of its kind quantitative framework to model amoeboid cell motion in 3D, and studies the role of both sub-cellular and extra-cellular parameters, there are a number of limitations in our model. First of all, we note that the computation of the critical surface tension is impossible because as the surface tension approaches the critical tension, the computation time becomes infinite. Also, as the channel becomes narrower, it becomes harder to simulate the cell because the cell elongates too long and meshing fails. Therefore, it is very hard to characterize the extreme behavior of the cell going through a narrow hole with strong surface tension. Also, in this simulation, the cell is treated as a viscoelastic Newtonian fluid. However, it is known from experiments that the cell has much more complex characteristics with cytoskeleton and organelles inside. It behaves nonlinear viscoelastic materials. Also, the cell membrane behaves in much more complicated ways too. Therefore, future studies will incorporate these more-complicated properties of the cell for more realistic simulations. In this simulation, the interactions between the cell membrane and matrix fiber is simplified. The non-slip condition between the extracellular fluid and the wall and existence of "inner" and "outer" surface of the wall mimic the friction between the cell membrane and matrix: as the rest distance, d_0 increases, the less friction between the cell membrane and the matrix fiber occurs. Also, in this simulation, the cell is treated as a passive liquid droplet in the pressure gradient. The cell does not generate any force by itself. Therefore, the simulation of the cell locomotion should be the next goal as well as the interactions between the cell surface and matrix fiber, such as the adhesion between these two surfaces. Despite these limitations, we believe that our simulation provides new insights that not only agree with current state-of-the-art experimental results but also predict results for future experiments. To date, the dynamics of cell centroid in 3D environments have not been fully probed. Our results predict how

the cell centroid speed would vary as a function of time and the size of the micro-channel. The effects of surface tension, viscosity and the size of the cell have also been predicted and would guide future experiments. We hope that our simulations will be a first step in guiding future experiments and experimental validations will further improve the accuracy of our predictions and enhance our understanding of complex modes of migration during tumor invasion and metastasis.

Acknowledgements

M.H. Zaman acknowledges the support of the National Institutes of Health (1R01CA132633-01A1).

References

[1] D. Bottino. How nematode sperm crawl. *Journal of Cell Science*, 115:367–384, 2001.

[2] K. Dahl, A. Ribeiro, and J. Lammerding. Nuclear shape, mechanics, and mechanotransduction. *Circ Res*, 102:1307–1318, 2008.

[3] M. Dembo. Hydrodynamics of micropipette aspiration. *Biophysical Journal*, 76:110–128, January 1999.

[4] P. Friedl. Amoeboid leukocyte crawling through extracellular matrix: lessons from the dictyostelium paradigm of cell movement. *Journal of Leukocyte Biology*, 70:491–507, 2001.

[5] P. Friedl. Prespecification and plasticity: shifting mechanicsms of cell migration. *Current Opinion in Cell Biology*, 16:14–23, 2004.

[6] P. Friedl and E. Brocker. Reconstructing leukocyte migration in 3d extracellular matrix by time-lapse videomicroscopy and computer-assisted tracking. *Methods Mol.Biol.*, 239:77–90, 2004.

[7] P. Friedl, K. Zanker, and E. Brocker. Cell migration strategies in 3-d extracellular matrix: differences in morphology, cell matrix interactions, and integrin function. *Microsc Res Tech*, 43:369–378, 1998.

[8] P. e. a. Friedl. Migration of highly aggressive mv3 melanoma cells in 3-dimensional collagen lattices results in local matrix reorganization and shedding of alpha2 and beta1 integrins and cd44. *Cancer Res.*, 57:2061–2070, 1997.

[9] V. Girault and P.-A. Raviart. *Finite Element Methods for Navier-Stokes Equations. Theory and Algorithms*. Springer Series in Computational Mathematics. Springer-Verlag, Berlin, Germany, 1986.

[10] D. Hanahan and R. Weinberg. The hallmarks of cancer. *Cell*, 100:57–70, 2000.

[11] J. Lammerding, K. Dahl, D. Discher, and R. Kamm. Nuclear mechanics and methods. *Methods Cell Biol*, 83:269–294, 2007.

[12] J. Lammerding and R. Lee. The nuclear membrane and mechanotransduction: impaired nuclear mechanics and mechanotransduction in lamin a/c deficient cells. *Novartis Found Symp*, 264:264–273; discussion 273–268, 2005.

[13] J. Lammerding and R. Lee. Mechanical properties of interphase nuclei probed by cellular strain application. *Methods Mol Biol*, 464:13–26, 2009.

[14] D. Lauffenburger and A. Horwitz. Cell migration: a physically integrated molecular process. *Cell*, 84:359–369, 1996.

[15] A. Mogilner. A simple 1-d physical model for the crawling nematode sperm cell. *Journal of Statistical Physics*, 110:1169–1189, 2003.

[16] A. Mogilner. The physics of filopodial protrusion. *Biophysical Journal*, 89:782–795, 2005.

[17] R. Rangarajan and M. Zaman. Modeling cell migration in 3d: Status and challenges. *Cell Adh Migr*, 2:106–109, 2008.

[18] A. Rowat, J. Lammerding, and J. Ipsen. Mechanical properties of the cell nucleus and the effect of emerin deficiency. *Biophys J*, 91:4649–4664, 2006.

[19] B. Rubinstein. Multiscale two-dimensional modeling of a motile simple-shaped cell. *Multiscale Model Simulation*, 3:413–439, 2005.

[20] J. Satulovsky. Exploring the control circuit of cell migration by mathematical modeling. *Biophysical Journal*, 94:3671–3683, 2008.

[21] D. Taylor, J. Condeelis, P. Moore, and R. Allen. The contractile basis of amoeboid movement. i. the chemical control of motility in isolated cytoplasm. *J.Cell Biol.*, 59:378–394, 1973.

[22] D. Taylor, J. Condeelis, and J. Rhodes. The contractile basis of amoeboid movement iii. structure and dynamics of motile extracts and membrane fragments from dictyostelium discoideum and amoeba proteus. *Prog.Clin.Biol.Res.*, 17:581–603, 581–603, 1977.

[23] D. Taylor, P. Moore, J. Condeelis, and R. Allen. The mechanochemical basis of amoeboid movement. i. ionic requirements for maintaining viscoelasticity and contractility of amoeba cytoplasm. *Exp.Cell Res.*, 101:127–133, 1976.

[24] A. Veksler. Phase transitions of the coupled membrane-cytoskeleton modify cellular shape. *Biophysical Journal*, 93:3798–3810, 2007.

[25] R. Weinberg. *Biology of Cancer*. Garland Science, 2006.

[26] K. Wolf and P. Friedl. Compensation mechanism in tumor cell migration: mesenchymal-amoeboid transition after blocking of pericellular proteolysis. *Journal of Cell Biology*, 160:267–277, 2003.

[27] K. Wolf, R. Muller, S. Borgmann, E. Brocker, and P. Friedl. Amoeboid shape change and contact guidance: T-lymphocyte crawling through fibrillar collagen is independent of matrix remodeling by mmps and other proteases. *Blood*, 102:3262–3269, 2003.

[28] K. Yoshida and T. Soldati. Dissection of amoeboid movement into two mechanically distinct modes. *J Cell Sci*, 119:3833–3844, 2006.

[29] M. Zaman. A multiscale probabilisitic framework to model early steps in tumor metastasis. *Mol Cell Biomech*, 4:133–141, 2007.

[30] M. Zaman, R. Kamm, P. Matsudaira, and D. Lauffenburger. Computational model for cell migration in three-dimensional matrices. *Biophys J*, 89:1389–1397, 2005.

[31] M. Zaman, P. Matsudaira, and D. Lauffenburger. Understanding effects of matrix protease and matrix organization on directional persistence and translational speed in three-dimensional cell migration. *Ann Biomed Eng*, 35:91–100, 2007.